

Active and Passive Control of Spar Vortex-Induced Motions

R. A. Korpus
Applied Fluid Technologies
326 First Street, Suite 34
Annapolis, MD 21043
410-703-2112
rkorpus@appliedfluidtech.com

S. Liapis
Shell International Exploration
and Production Company
3737 Bellaire Blvd.
Houston, TX 77025
713-245-7677
Stergios.Liapis@shell.com

Spars have become an “Industry Solution” for deepwater developments. Vortex-Induced Motion (VIM) of spar platforms in currents remains an important design concern. While strakes are effective at suppressing riser VIM, all three straked classical spars in the Gulf of Mexico have experienced significant VIM events. These are not examples of poor design but indicate a lack of adequate tools for predicting Spar VIM. This paper presents the development and validation of Unsteady Reynolds-Averaged Navier-Stokes (URANS) methods to predict real-world spar VIM behavior. It includes the ability to address rough surfaces and high super-critical Reynolds numbers. The resulting algorithms are used to assess the effectiveness of active and passive control strategies for suppressing spar VIM. Active control consists of injecting high-pressure water tangentially into the boundary layer, and is shown to be extremely effective at reducing drag and VIM amplitudes. Passive control utilizes a sleeve to channel high-pressure stagnation flow into the boundary layer, and is found less effective.

Introduction

Spars have become an “Industry Solution” for the deepwater Gulf of Mexico. Yet there continue to be technical issues with the Spar concept pertaining to Vortex-Induced Motions (VIM) in currents. The awareness and potential consequences for mooring line or riser failure due to hull VIM has come front and center with the openly reported experiences of the Genesis and Diana-Hoover Spars, and now shows bright on industry’s radar screen as an area requiring additional research. All three spars currently installed in the Gulf of Mexico experience occasional large VIM events even though they have strakes.

In the case of the Genesis spar, the mooring system was designed for VIM amplitudes equal to 20% of the spar diameter. During the period 1999-2002, the spar experienced VIM under eddy events with estimated velocities around 1.5 to 2 knots. The maximum observed amplitude was about 38% of the diameter, about double the design value. As a result of VIM motions, and due to concern for mooring fatigue and wear at the fairlead, the operator had to replace the 1000’ chain upper segment of three mooring lines. They also plan to implement a “step tensioning” operational procedure activated during severe current events in an attempt to mitigate any future VIM occurrences. In the case of the Neptune spar, VIM has been recorded in the field with maximum amplitude equal to 32% of the diameter. The third classic spar in the Gulf of Mexico, Hoover-Diana, has also experienced VIM events with maximum VIM amplitude of 48% of the diameter.

It is important to realize that these examples of excessive VIM are not indicative of poor design, but rather of a lack of adequate tools for predicting VIM. The problem is extremely difficult because scale effects make model testing nearly impossible, and flow complexity taxes the ability of most computational approaches. The flow is viscous, unsteady, and

dominated by strong vortices created by separating boundary layers [1-6]. The large diameters and marine environment necessitate post-critical Reynolds numbers and rough surfaces, and thereby add to turbulence model complexity [7-13]. Additional demands are also dictated by the requirement for more sophisticated validation data.

Perhaps the best approach for understanding VIM is the computational method known as Reynolds-Averaged Navier-Stokes (RANS). RANS accurately models unsteady, viscous, vortex-dominated flow, and provides sufficient flexibility to accommodate super-critical Reynolds numbers and rough surfaces. RANS codes have been successfully applied to numerous fluid/structures interaction problems [14, 15] and to meet the demands real-world design applications [16, 17].

But the problem of spar VIM pushes even RANS to its limit. The simultaneous demands of high super-critical Reynolds number, moving bodies, unsteady flow, and rough surfaces lie beyond what most RANS codes can handle. The main tool used in this study, therefore, is an overset grid-based RANS code developed specifically for fluid/ structures interaction problems. It has been validated at Reynolds numbers up to 10^9 [16, 18], and contains some of the most sophisticated roughness models currently available.

The work presented herein addresses development of two alternative VIM control strategies using RANS as design tool. The first consists of actively injecting fluid in a direction tangential to the spar. The second strategy is passive, and based on adding an external sleeve. The effectiveness of each scheme is assessed, and a parametric study undertaken to find the best configuration. The main conclusion is that active injection is highly effective, and can reduce drag and oscillation amplitude by large factors. Passive control was also found to reduce VIM but not as effectively as active injection.

Approach

The motion of fluid at high Reynolds number is simulated using the three-dimensional, unsteady, incompressible Reynolds-averaged Navier-Stokes (RANS) equations. In vector form the dimensional versions are:

$$\nabla \cdot \mathbf{V} = 0 \quad (1)$$

$$\frac{\partial \mathbf{V}}{\partial t} + \mathbf{V} \cdot \nabla \mathbf{V} + \frac{1}{\rho} \nabla p - \nabla \cdot \boldsymbol{\tau} + g\mathbf{k} = 0 \quad (2)$$

The Cartesian vector \mathbf{V} represents flow velocity, t is time, ρ is fluid density, and p its local static pressure. Gravity, g , and its direction, \mathbf{k} , are included so that free surfaces can be modeled.

The shear stress tensor $\boldsymbol{\tau}$ includes both mean and turbulent components, and therefore requires turbulence models for closure. The usual assumptions for Newtonian fluids give:

$$\tau_{ij} = -\frac{2}{3}k\delta_{ij} + \nu S_{ij} + \overline{u_i' u_j'}, \quad S_{ij} = \frac{\partial u_i}{\partial x^j} + \frac{\partial u_j}{\partial x^i} \quad (3)$$

Here, S_{ij} represents the tensoral strain of mean flow, ν the viscosity, k the isotropic turbulent kinetic energy, and overbarred terms the turbulent Reynolds stress components. The quantities u^i ($i=1,3$) are Cartesian components of \mathbf{V} , and x^i ($i=1,3$) are components of the Cartesian position vector.

Reynolds stresses are provided using eddy viscosities computed from one length scale and one time scale. All results presented herein are made with both scales calculated from additional convection/diffusion equations; except in the viscous sublayer where the time scale is computed algebraically. The resulting $k\varepsilon$ model solves the equations:

$$\frac{\partial k}{\partial t} + \mathbf{V} \cdot \nabla k - \left(\frac{1}{\text{Re}} + \nu_t \right) \nabla^2 k - P + \varepsilon = 0 \quad (4)$$

$$\frac{\partial \varepsilon}{\partial t} + \mathbf{V} \cdot \nabla \varepsilon - \left(\frac{1}{\text{Re}} + \frac{\nu_t}{1.3} \right) \nabla^2 \varepsilon - c_1 \frac{\varepsilon}{k} P + c_2 \frac{\varepsilon^2}{k} = 0 \quad (5)$$

k is now the turbulent kinetic energy, ε its dissipation rate, P its production from mean strain, and ν_t the eddy viscosity. Re is Reynolds number; c_1 and c_2 are modeling coefficients. The accompanying near-wall model solves the first equation, but computes ε from algebraic relations involving vorticity and distance to the wall. Details of the near-wall model and values for c_1 and c_2 can be found in Chen and Korpus [19]. Switching between models occurs when y^+ exceeds 20.

Although simpler and more efficient models exist, none are known to be universally reliable for the types of flows studied here. Zero-equation models (such as Baldwin-Lomax) are robust and easy to use, but are not particularly accurate in adverse pressure gradients or weak separation regions. One-equation models (such as Spalart-Almaras) have demonstrated better success with bluff-body flows, but still trade physical accuracy (the time scale) for robustness. Since the two-layer

model described above proves robust for many diverse flow types, we feel there is no reason to revert to simpler models.

Wall functions have been explicitly avoided for similar reasons. While such boundary conditions greatly simplify implementation of roughness models (and reduce grid size), the assumptions upon which they are based are not valid at separation [20, 21]. Since drag and VIM response are closely related to wake width, any approximations that limit the accurate prediction of separation should be avoided at all cost.

Computations around complex geometries require the primitive variable and turbulence quantity equations be transformed into body fitted coordinates. Discretization is accomplished in the transformed system by linearizing each equation over a single computational cell, and solving analytically by separation of variables. Evaluation of the analytic solution at the interior node of a computational element provides a stencil for the center point in terms of its nearest neighbors. Time derivatives are handled by the Euler implicit method, and the algebraic system solved by the alternating direction implicit (ADI) method in each cross-flow plane [19, 22]. Detailed expressions for the difference stencil can be found in Chen et al. [20, 22]

Simulations involving multi-component geometries and moving bodies are handled by embedding the discrete equations in a multi-block overset-grid environment. The solver works on one block at a time, and the only grid connectivity requirement is that the union of blocks spans the entire computational domain. Individual blocks are allowed to overlap arbitrarily, and inter-block communication is handled by conservative tri-quadratic interpolation. The overall approach is extensively validated for both steady and unsteady three-dimensional applications [14-18, 23]

Free-motion (VIM) cases are handled using a combination of near-field body-fitted grid blocks, and far-field Cartesian grid blocks. Near-wall blocks are moved at each time step to coincide with displacements found by solving the VIM equations for x and y motion. Cylinder mounts (as would be required in an experiment) are not modeled. The VIM equations include terms for cylinder mass, mooring system tension, and (if desired) mooring system damping. Hydrodynamic forcing is computed by integrating RANS pressure and skin friction after every time step. The VIM equations are advanced explicitly in time to provide grids for the next RANS iteration. Communication between blocks is provided by interpolation after every time step.

Roughness modeling is handled by combining the concept of distributed force fields to represent roughness element drag [24, 25], and increases to Turbulent Kinetic Energy (TKE) creation to represent roughness element separation. Both terms are important because additional turbulent energy accounts for skin-friction increase, whereas roughness element drag accounts for early separation in adverse pressure gradients. Because the two terms do not always work in unison, modeling their action using a single factor (such as wall functions) cannot properly account for

these independent effects. Element drag is incorporated by adding source terms proportional to roughness height and local velocity-squared to the momentum equations. TKE production effects are modeled by adding source terms proportional to mean kinetic energy in the TKE equation. Both modifications start at the wall, and extend to the extreme of roughness height.

Both of these modifications are necessitated by the physics of rough surface boundary layers [8, 9, 26]. Many classic references [27, 28] refer to a simple downward shift in the log-region of the boundary layer, but such a method is insufficient for practical applications. It provides no insight into the boundary layer profile in the viscous sub layer, and can therefore only be applied using wall functions in the log layer. As mentioned earlier, reliance on wall functions can be expected to introduce inaccuracies for separated flows.

An additional problem with the use of simplified roughness models becomes obvious when one considers typical boundary layer thickness on offshore platforms. Spar platform in two knots of current, for example, have boundary layers ranging from less than 3 centimeters thick 45 degrees aft of the nose, to 6 cm thick at 90 degrees. Even 3 cm of roughness ($k/D = .001$) protrudes through the boundary layer. Any model that assumes all-important interactions take place within the inner log-region will lead to inaccuracy. Roughness height has been assumed on the order of $k/D=0.002$ for all the results in this paper.

The current roughness model can account for both increases in skin friction and decreases in separation resistance. A good test of the former is shown in Figure 1, which gives comparisons between flat-plate calculations and the classic Moody diagram [28]. Only two lines are shown for clarity: a smooth plate; and one with constant roughness equal to $k/L = 0.001$. Corresponding RANS results are shown at discrete Reynolds numbers.

The model's ability to account for more complex effects is demonstrated in Figure 2. The plot shows boundary layer profiles in the y^+, u^+ coordinate system. Symbols indicate Spalding's curve fit to available (smooth-plate) experimental data, and RANS calculations show remarkable agreement.

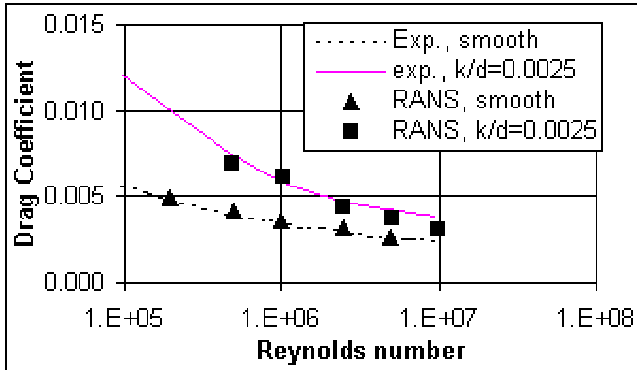


Figure 1: Roughness Model Validation – Flat Plate Drag

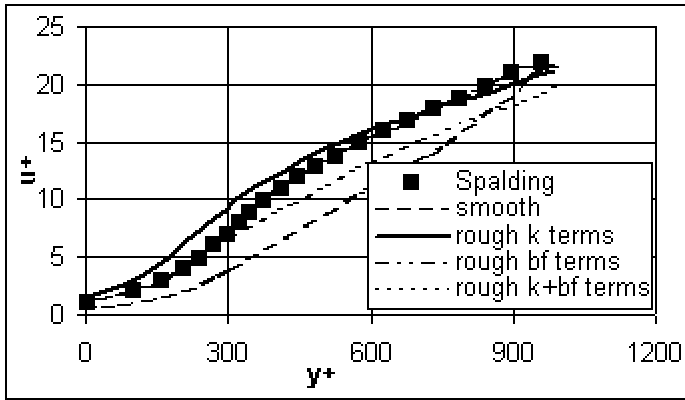


Figure 2: Roughness Model Validation – Boundary Layer Profile

Also included are RANS results with various portions of the roughness model activated. The curve generated using only turbulent energy terms (labeled 'k terms') shows an increase in wall shear, but at the expense of violating the relation $\tau = \mu du/dy$ (implicit in the sub layer relation $u^+ = y^+$).

The curve generated using only momentum equation body forces (labeled 'bf terms'), shows a reduction in wall shear, but again at the expense of the skin friction relation. It also exhibits the problem, common to most simple roughness models as noticed by Cebeci [27], that the theoretical parallelism of boundary layer profiles in the log region is lost. Only results with both turbulence and body force terms captures sublayer behavior and log region slope correctly.

In addition to these roughness model improvements, two additional methodologies are employed to insure accurate VIM calculations. The methods constitute a standard quality assurance procedure that should be employed with all computational applications – the assurance of grid and time step independence. A number of progressively finer grids are developed, and run through the same simulation. Proper resolution is found when the resulting force predictions stop changing with grid resolution. The procedure must be repeated using progressively smaller time steps if the application is intended to be time-accurate.

Validation 1 – Stationary Cylinders

Performance of the described roughness model for separated flows is best demonstrated using two-dimensional, fully turbulent circular cylinder test cases. Three series of calculations was made to support this validation: smooth cylinders; moderately rough cylinders ($k/D = 0.0002$); and fully rough cylinders ($k/D = 0.002$). Each series spans a range of post-critical Reynolds numbers from 300,000 to 7,000,000. A fourth series was made at high sub-critical Reynolds numbers to provide comparisons with laminar flow cylinders.

Plots of vorticity at one Reynolds number and a single instant in time are shown in Figures 3, 4, and 5. Figure 3 depicts a sub-critical case with laminar boundary layer and no

roughness. Figures 4 and 5 depict post-critical flow, and show smooth and rough cylinders respectively. Figures 6, 7, and 8 show corresponding close-ups of the boundary layer profiles near separation. As expected, the sub-critical cylinder exhibits very thick boundary layers and separates upstream of the 90-degree point. The early separation creates a thick and strong vortex wake. By comparison, the post-critical smooth cylinder has a very thin boundary layer that separates downstream of the 90-degree point. Its vortex wake is thinner and appears more stretched in the freestream direction.

The post-critical, rough cylinder wake (figure 5) appears more like a laminar flow than a turbulent one. But it is interesting that corresponding boundary layer profiles (Figure 8) don't look anything like other presented cases. Separation occurs downstream of the 90-degree point (like other turbulent cylinder flows), but the profile looks more like a cross between turbulent and laminar flows. The outer portion is full like a turbulent one, but the inner part looks laminar due to a reduction in velocity caused by roughness element drag. Boundary layer thickness is many times greater than smooth-surface post-critical cylinder flows. The end result is a wider wake, and separation cavity pressure acting over a larger region. Thus, even though skin friction increases only slightly by roughness, total drag increases substantially.

Post-critical smooth and rough cylinder simulations were made at Reynolds numbers of 300,000, 600,000, 1,000,000, and 7,000,000. The hydrodynamic force perpendicular to current direction (hereafter referred to as transverse force) was monitored throughout the calculation for the purposes of defining convergence. Convergence is considered obtained when all startup transients have died away, and the time history of transverse force reaches a purely oscillatory state of constant amplitude and period. Each simulation was then continued for 5 - 10 more force oscillations for the purpose of computing its response statistics. Cases with more monotone or narrow-band responses required fewer additional periods, whereas cases with more broadband response were run longer to achieve more complete statistical data sets.

Drag values were computed from each run by integrating pressure and skin friction, and then averaging over the post-convergence oscillations. The resulting values are plotted along with high Reynolds number experimental data of Deng [29] in Figure 9. Experimental and computational results overlap in the Reynolds number range $300,000 < Re < 1,000,000$, and indicate that both smooth and moderately rough RANS results are fairly accurate.

There is one area where the comparisons are not as good. Large roughness ($k/D = 0.002$) combined with high Reynolds number ($Re > 500,000$) result in under-prediction of drag by as much as 20%. The combination causes roughness elements to protrude into freestream flow, and the simplistic approach of adding drag and turbulent kinetic energy becomes incapable of resolving the complex physics. More work is needed to refine the roughness model, but it would also prove

enlightening to compare the present work to predictions made by LES or DES simulations.

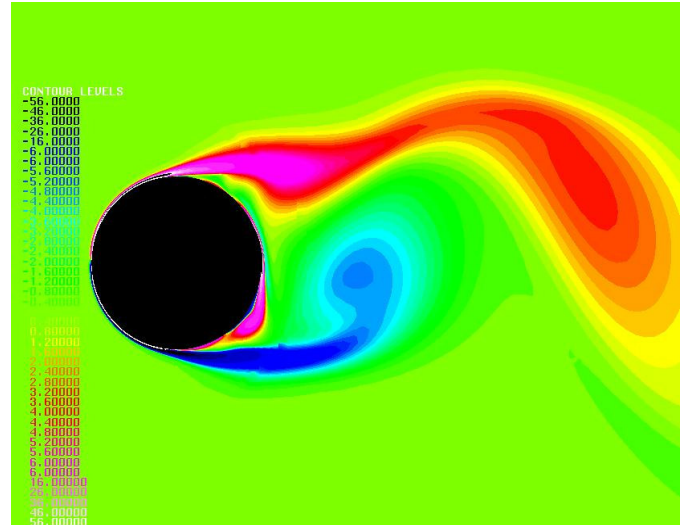


Figure 3: Vorticity Behind a Smooth Cylinder at $Re=10,000$

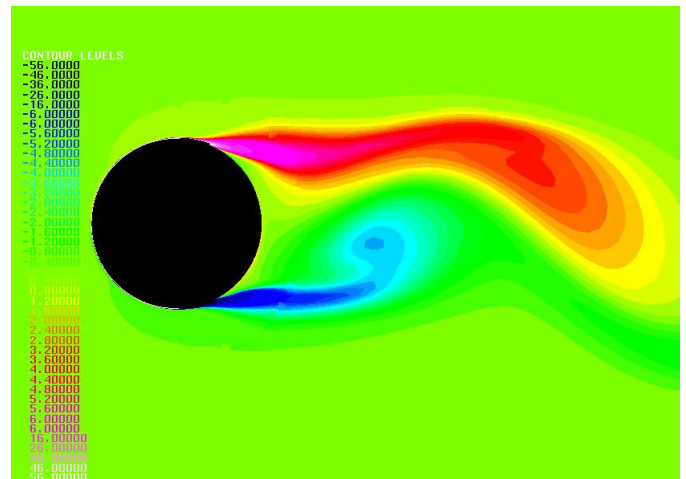


Figure 4: Vorticity Behind a Smooth Cylinder at $Re=7,000,000$

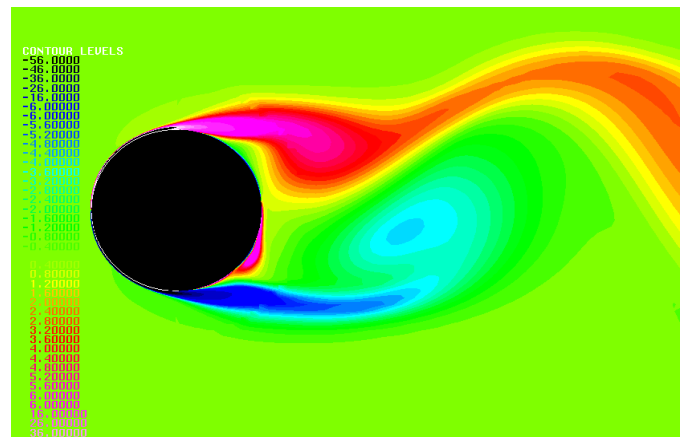


Figure 5: Vorticity Behind a Rough Cylinder at $Re=7,000,000$

Validation 2 – Moving Cylinders

A second level of validation is required before RANS can be applied to design VIM mitigation devices. In addition to the drag force accuracy, VIM simulation requires the reliable prediction of transverse force amplitude and phase. Force amplitude is important because it determines the amplitude of motion response, and phase is important because it determines when VIM “lock-in” will occur. Lock-in is the phenomenon wherein hydrodynamic added mass lies in a range where platform natural frequency and Strouhal shedding frequency align. VIM only achieves meaningful amplitudes in this resonant range, so its accurate prediction is important.

Previous studies [15] have shown that RANS can predict VIM quite accurately for smooth cylinders at sub-critical Reynolds numbers. But little validation is available at higher Reynolds numbers or with rough cylinders. Three additional studies were undertaken to supplement currently available validation experience: a $Re = 100,000$ rough cylinder series; a $Re=10,000,000$ smooth cylinder series; and a $Re = 10,000,000$ rough cylinder series. Each covers a reduced velocity range from 3 to 12.

Typical time histories of transverse force and cylinder displacement are shown in Figure 10 and 11 respectively. All curves represent simulations performed using a system natural frequency corresponding to reduced velocity $V_r = U_{freestream}T / D = 6$, where T is the system natural period accounting for spar mass and mooring stiffness, but not hydrodynamic added mass. Rough simulations were all performed with $k/D = 0.002$. Only converged portions of the histories are shown.

It is interesting to note that even though drag force is highly sensitive to Reynolds number and roughness (Figure 9), transverse force is not. Even for the large variations considered here, the four transverse force amplitudes are all within 20% of each other. Transverse displacement, however, is highly sensitive to Reynolds number and roughness. Figure 11 shows that rough cylinders always experience more motion than smooth, and low Reynolds number flows always induce more motion than high. The range spans $A/D = 0.3$ to 0.7 .

A comparison of phase between corresponding curves in Figures 10 and 11 shows that for $V_r = 6$, the force is always close to 180 degrees out of phase with displacement (i.e. in phase with acceleration). This indicates that the hydrodynamic force exhibits very little damping, and consists almost entirely of negative added mass. The cumulative effect is similar to a driving force in conventional forced vibration problems, and is consistent with lock-in. This is expected at reduced velocities of 6. Careful observation also shows that each of the four cases has slightly different period (due to the effect of added mass). Although the prescribed mooring system natural period is 213 seconds, response periods are substantially less as shown in Table 1.

Comparisons between the RANS-predicted transverse response ratios and available experimental data are shown in Figure 12. For the low Reynolds number, smooth cylinder

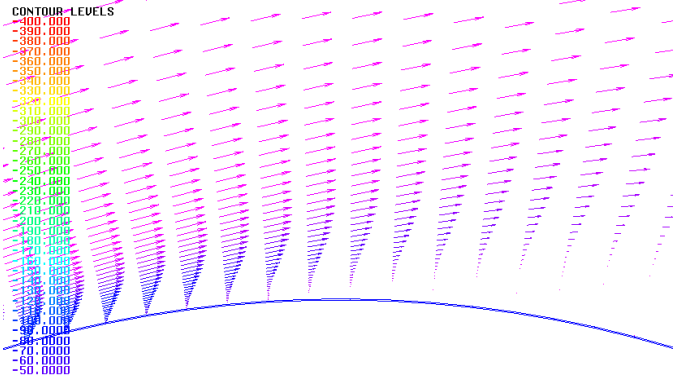


Figure 6: Velocity (Colored by Vorticity), Smooth at $Re=10^4$

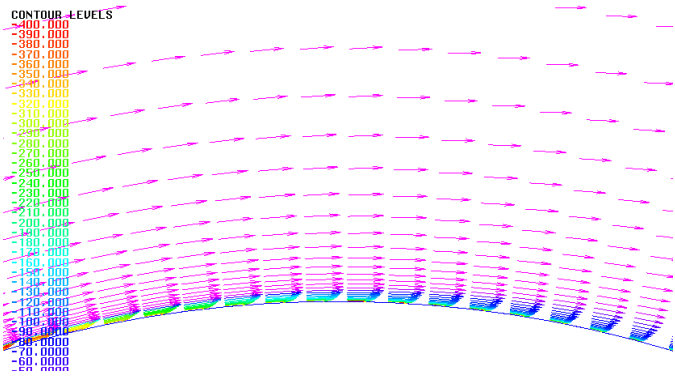


Figure 7: Velocity (Colored by Vorticity), Smooth at $Re=7 \times 10^6$

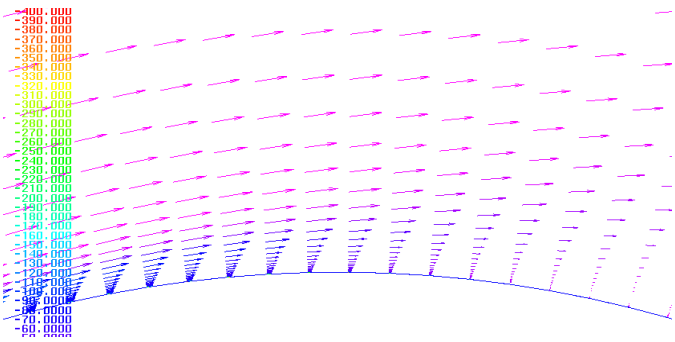


Figure 8: Velocity (Colored by Vorticity), Rough at $Re=7 \times 10^6$

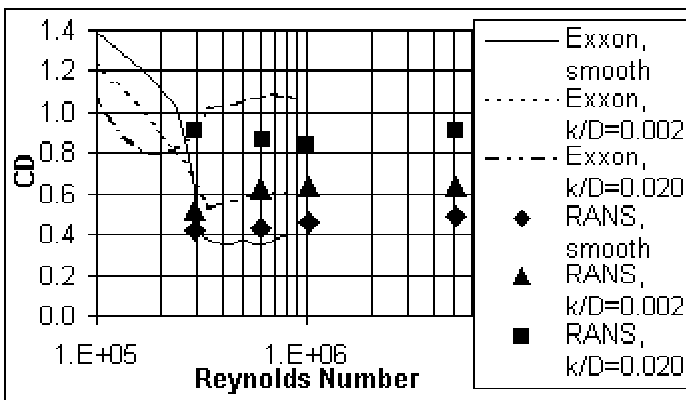


Figure 9: Drag of Stationary Rough Cylinders

Active and Passive Control of Spar Vortex-Induced Motions

case, the experimental data of Hover [30] are included. Note that the corresponding RANS diamonds always fall within 0.1 of A/D of the Hover data (labeled 'MIT'). For the high Reynolds number, rough cylinder case, the experimental data of Ding et al. [29] is included. Ding's measurements are labeled 'Exxon' in the plot, and correspond to the RANS squares. Above a reduced velocity of 5 the comparison is quite favorable. Unfortunately the RANS predictions show large A/D response down to a reduced velocity of 3, and indicate that RANS has some difficulty getting the phase shift of lock-in to occur at exactly the right frequency.

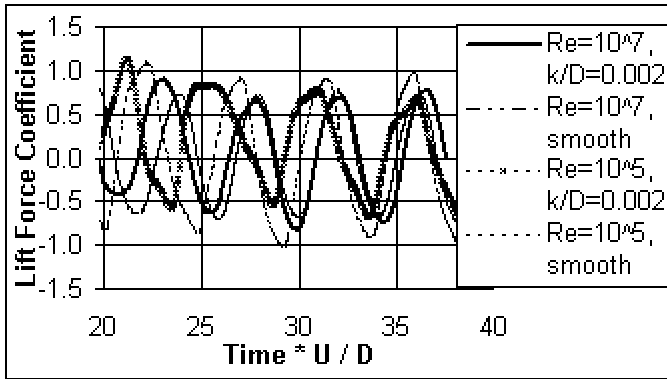


Figure 10: Time History of Bare Cylinder Transverse Force

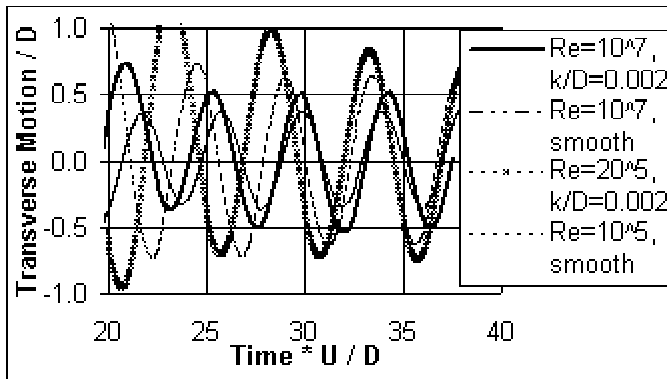


Figure 11: Time History of Transverse Displacement

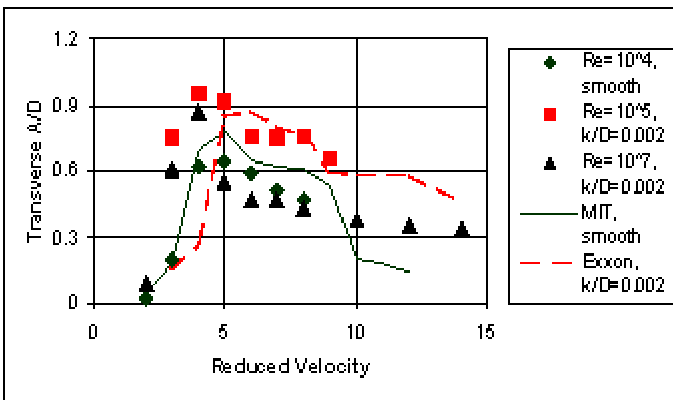


Figure 12: Cylinder VIM versus System Reduced Velocity

Table 1: Comparison of Response Period

	smooth	rough
Re = 100,000	160 seconds	147 seconds
Re = 10,000,000	180 seconds	161 seconds

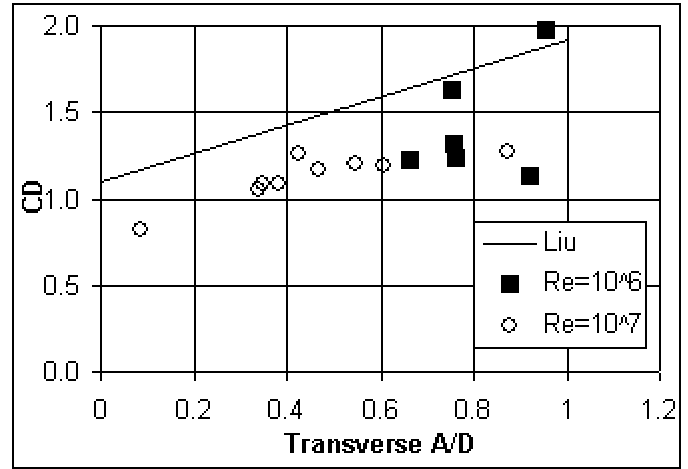


Figure 13: Drag vs. Displacement for Bare Cylinders

Figure 12 also includes the RANS data for high Reynolds number rough cylinders (labeled with triangles). Note that at reduced velocities above 5 the predictions appear more like the low Reynolds number smooth data than the moderate Reynolds number rough data. Reynolds number apparently has greater impact on VIM amplitude than roughness, even when comparing post-critical to post-critical flows. The high Reynolds number, rough cylinder predictions also exhibit a possible phase error down to reduced velocities of 3.

One final validation comparison can be made using the data of Liu et al. [31]. The authors proposed a “rule of thumb” for predicting Spar VIM drag as shown in Figure 13. Since they developed their model using a roughness height of $k/D = 0.002$, we include only that RANS data for clarity. The comparison draws conclusions similar to those of Figure 9 – that for cases involving high Reynolds number and large roughness, RANS under-predicts drag by as much as 20%.

VIM Mitigation by Active Injection

The above comparisons demonstrate that for the most part, RANS is an accurate VIM modeling tool and can be reliably applied to design VIM mitigation concepts. The first such concept under consideration is tangential injection of the boundary layers at ± 90 degrees from the cylinder's upstream position. The concept is termed “active injection” because power must be applied to build up sufficient pressure. Pumping seawater into an internal plenum generates pressure, which then drives the boundary layer vents via internal piping.

Active injection has been studied extensively in the field of aerodynamics as a means of delaying separation on airfoils. The idea was first applied to spar VIM by Shu and Allen, and is described in their patent application [32]. Schultz et al. [33]

used low-Reynolds number numerical studies to assess the scheme's effectiveness. Brown et al. [34] provided experimental verification of this idea.

The concept is best demonstrated by Figure 14, which shows a close-up of the computational grid in way of the boundary layer injection vents. Three separate grid blocks are indicated: a red one for resolving the upstream exterior boundary; a green one for the downstream exterior boundary layer; and a blue one for the vent itself. The blue block actually extends some distance inside the cylinder to physically separate injection plenum boundary conditions from the vent exit/mixing region. The separation is necessary because the plenum requires high pressure to drive the flow, but must exit into relatively low static pressure in the surrounding fluid. Velocity at the plenum end is specified, but pressure is computed as part of the solution.

Figure 15 shows a snapshot of velocity (colored by pressure) at one instant in time from a case where the injection velocity is 4 times freestream current speed. The vent exit over-velocity is clearly visible, as is its ability to create a strongly attached boundary layer downstream.

The pressure gradient computed inside the vent is indicative of the energy needed to drive the flow, and appears quite strong. Pressure in the figure is non-dimensionalized by ρU^2 (where U is current speed), and indicates plenum pressure must be 18 times stagnation pressure in order to drive the flow. While this may seem excessive, it dimensionalizes to only 1.5 psi over hydrostatic pressure for a 2-knot onset current.

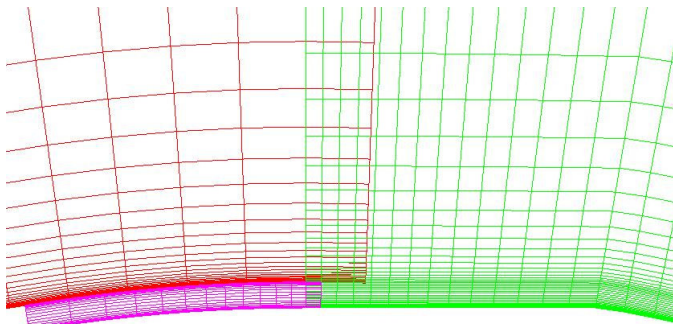


Figure 14: Computational Grid Around Injection Outlet

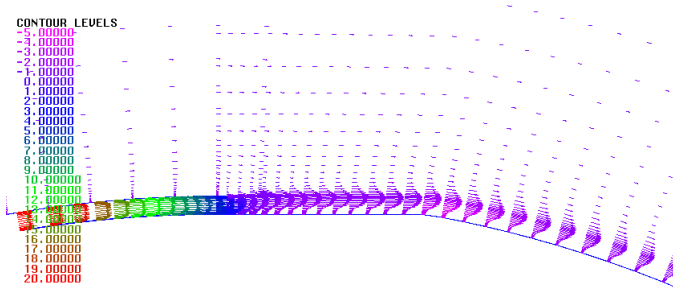


Figure 15: Velocity (Colored by Pressure) Around Injection Outlet

A number of different design variables were investigated to study performance of this mitigation concept. The test matrix consists of two exit-vent opening heights (0.005D and 0.0075D), two reduced velocities (4 and 6), and 5 injection velocities (0, 2, 4, 6, and 7 times current speed). A roughness height of $k/D = 0.002$ was used for all cases, and the Reynolds number left fixed at 7,000,000. Current direction for most simulations was fixed to place the exit vents symmetrically on the Spar. A small number of off-design cases were run to simulate the effect of a 10 degree off-axis current.

A typical set of results is shown in Figures 16 through 19. The figures depict contours of vorticity at one instant in time from each of four injection speeds. Each derives from simulations utilizing a gap of 0.0075D and reduced velocity of 6. Figure 16 shows the case with injection velocity at two times freestream; Figure 17 shows 4 times freestream; 18 is 6 times freestream; and 19 is 7 times freestream. Cylinders do not necessarily coincide with figure centerlines since some of them are experiencing VIM.

The effect of injection on vortex wake is dramatic. The two times freestream-injection case (Figure 16) looks similar to Figure 5 for bare circular cylinders. This is not unexpected since the local flow velocity in the absence of injection is already two times freestream. Two times injection merely adds fluid at the same energy level as the local boundary layer. Four times injection, however, thins the wake considerably, and makes it look more like the high Reynolds number smooth cylinder case of Figure 4. By the time injection velocity reaches six times freestream, the wake begins to look more like a “waving tail” than a von Karman vortex street. The ultimate mitigation device is achieved with seven times injection, where all asymmetry and unsteadiness in the wake has completely disappeared.

Time histories of displacement and force corresponding to the first three of these simulations are shown in Figures 20 through 23. Figure 21, for example, shows an interesting trend. The average drag is seen to decrease with injection velocity (as evident from the reduction in mean displacement), but the amplitude of unsteadiness to the drag history actually increases. The reason for this becomes obvious in Figure 23. An increase in injection velocity causes the drag oscillation period to increase. Thus, even though drag oscillation amplitude reduces, the excitation comes more into line with mooring system natural frequency.

Results for the complete design series are shown in Figures 24 and 25, which present transverse displacement A/D and drag coefficient respectively. Each figure includes curves for both gap ratios, and contains isolated points for the off-axis current cases. The effect of injection is dramatic. At just four times freestream injection reduces VIM amplitude by a factor of five and drag by a factor three. At six times freestream the reduction factors are 10 and 4 respectively. Finally, it should be noted that since these reductions are due mostly to interactions in the downstream wake, it would be informative to check these simulations using a DES technique.

Active and Passive Control of Spar Vortex-Induced Motions

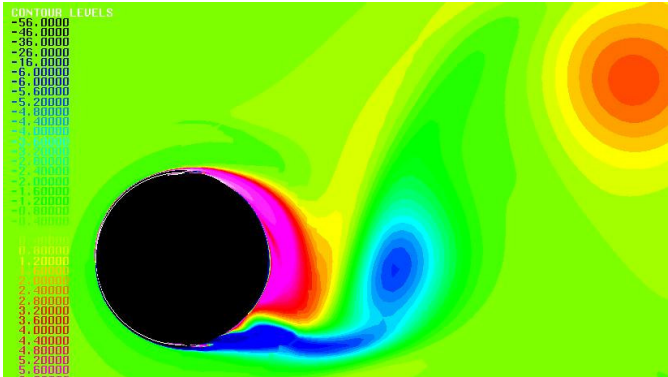


Figure 16: Vorticity for $V_{INJ} = 2 \times$ Freestream

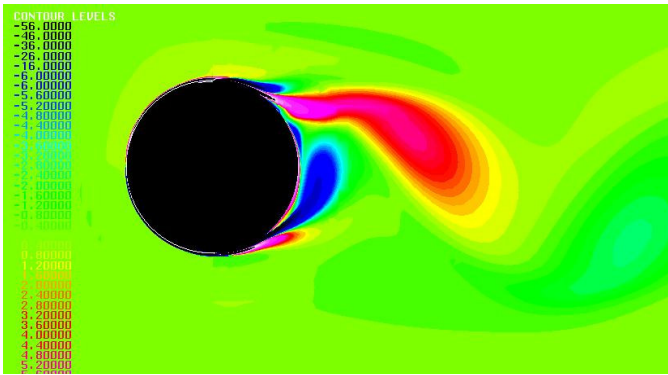


Figure 17: Vorticity for $V_{INJ} = 4 \times$ Freestream

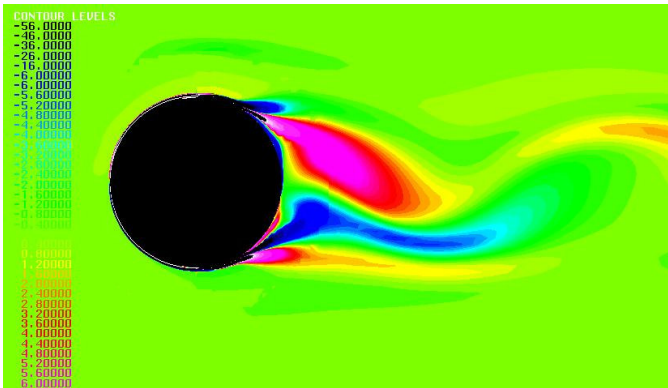


Figure 18: Vorticity for $V_{INJ} = 6 \times$ Freestream

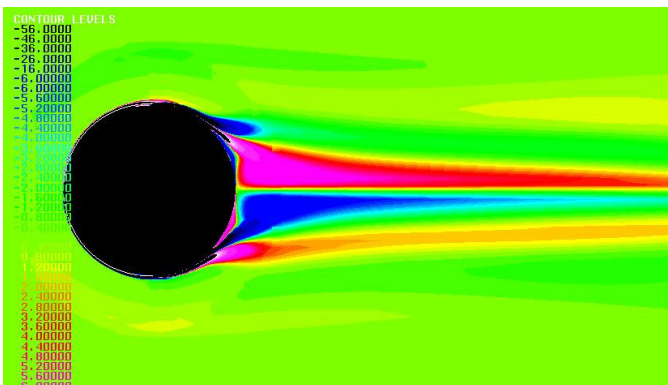


Figure 19: Vorticity for $V_{INJ} = 7 \times$ Freestream

Since all simulations were performed using the highest roughness level, these results are likely indicative of real-world spar geometries (i.e. including anodes, chain fairleads, etc.). It is important, however, that the minimum drag coefficients shown in Figure 25 are not used for design. Mooring system ultimate strength should still be governed by no-injection drags like those shown in Figures 9 (stationary spars) and 13 (moving spars).

An elementary estimate of the power required for pumping injection water gives:

$$Power = [\rho(U_{INJ})^3(gap)/2 + P(U_{INJ})(gap)] * L \quad (6)$$

Where P is the plenum pressure required for driving injection and L is the length of slot required. In the interest of checking the practicality of active injection, consider the case of a 36.6 meters diameter spar in 3-knots of current. Elimination of VIM, as Figures 24 & 25 suggest, requires injection velocities of at least six times current speed, (9.3 meters per second). Required Plenum pressure is 21.7 KPa. If a gap of 0.005 diameters (18.3 cm) is used, required power is 114 kilowatts per meter of slot. Current events are typically fairly shallow, so we can reasonably assume that only the 60 meters of spar closest to the free surface would require suppression. In such a case the total amount of required power is 13,600 kilowatts. Compared to the total installed electrical power onboard a spar, this constitutes a rather modest requirement.

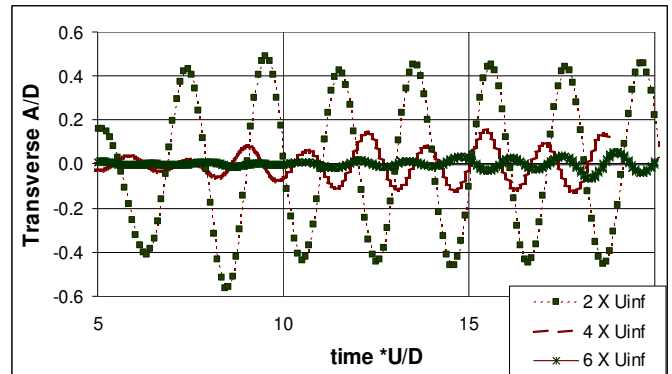


Figure 20: Effect of Injection on Transverse Displacement

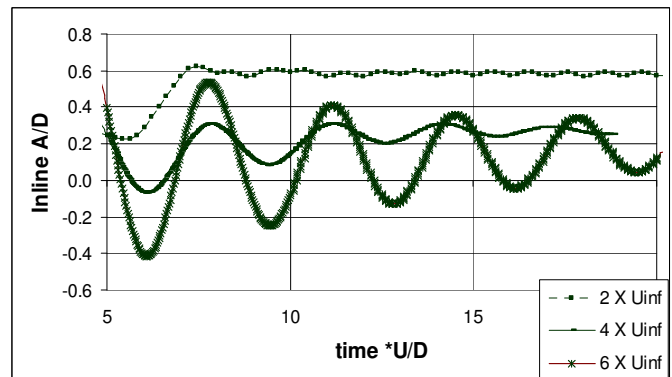


Figure 21: Effect of Injection on Inline Displacement

VIM Mitigation by Passive Injection

The second VIM mitigation concept addresses a design idea intended to provide boundary layer injection without the need for active power input. The concept utilizes an exterior sleeve placed around the sides of the Spar that channels high-energy flow from the frontal stagnation point to the boundary layer separation point. The scheme was patented by Shu and Allen [35], and is described schematically in Figure 26. Flow enters the sleeve from its upstream end, and therefore at low speed but high (near stagnation) pressure. Since the flow exits the sleeve into relatively low ambient pressure, substantial pressure gradient is available to drive flow through the sleeve. The channel's outer wall adds energy by turning the flow rather than allowing it to separate. As long as the angle of attack is small, there is no possibility of galloping instabilities.

The number of possible design combinations for this concept is quite large. Any of the variables shown in Figure 26 could change over a relatively large range of values. The current investigation has therefore been limited for practical reasons to varying only the outlet angular location θ . Values of t , e , T , and r remain fixed throughout this study at $0.05D$, $0.10D$, $0.05D$, and $0.25t$, respectively. Studies were conducted at reduced velocities of 4 and 6, but only rough ($k/D = 0.002$) and high Reynolds number ($Re = 7,000,000$) cases were considered. Off-design functionality was studied by performing simulations with onset current misaligned from the cylinder axis by 10 degrees.

Figure 27 presents contours of vorticity for the case of reduced velocity 6. Distinct vortices are seen to arise both from flow in the sleeve exits, and from boundary layers separating on the outside sleeve surface. The wake is more complex than previous examples, and not symmetric. Von Karman shedding has not been suppressed.

Figure 28 shows a close-up of streamwise velocity inside the channel. The concept is seen to work fairly well in that even though flow enters at low speed, it achieves values in excess of 1.4 times freestream by the channel exit. Unfortunately, the exterior flow velocity (outside the boundary layer) at that location is about this same value, and little net energy is added from the channel.

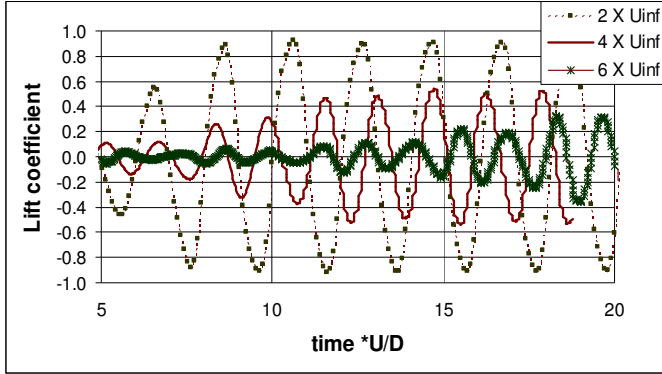


Figure 22: Effect of Injection on Transverse Force

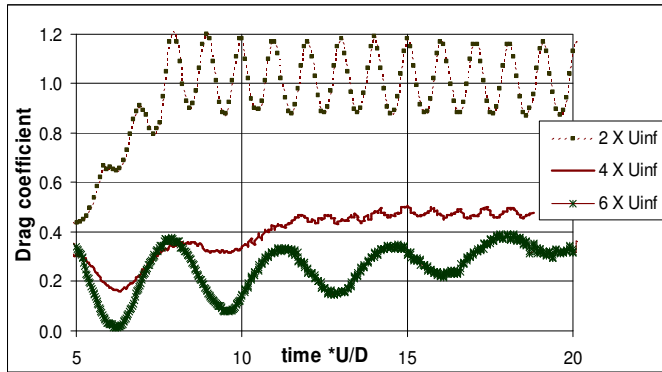


Figure 23: Effect of Injection on Inline Force

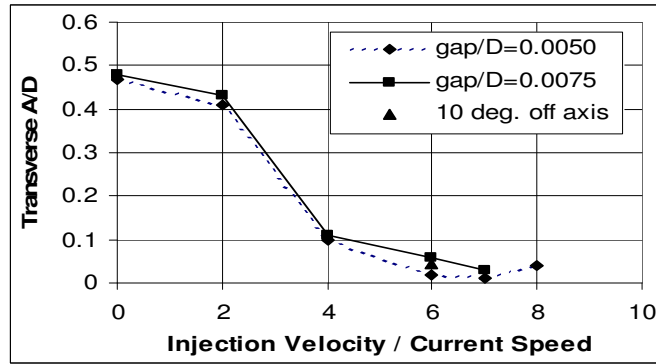


Figure 24: Transverse Amplitude versus Injection Velocity

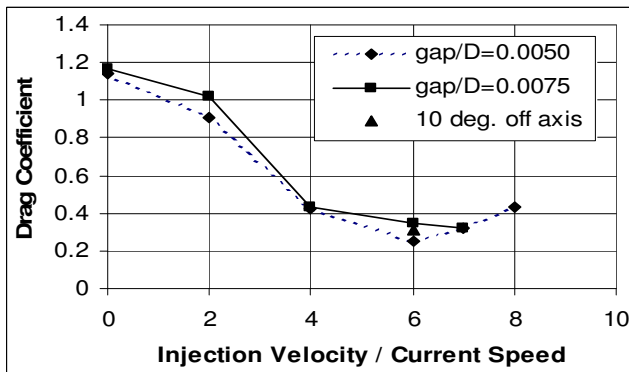


Figure 25: Drag versus Injection Velocity

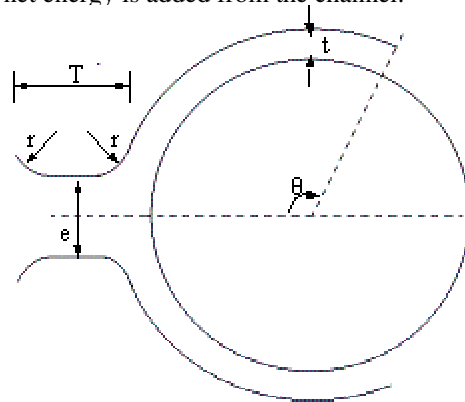


Figure 26: Passive Injection Sleeve Geometry

Active and Passive Control of Spar Vortex-Induced Motions

We should therefore expect a behavior similar to 2 x freestream injection. Figures 29 and 30 show close-ups of the inlet and outlet flow respectively. The first shows velocity magnitude at the inlet, and demonstrates only very small regions of low speed flow or separation (e.g. near the outer surface of the sleeve inlet). Figure 30 shows velocity vectors (colored by velocity magnitude), and indicate that sleeve exit flow is fairly strong. Given that low speed inlet flow is required to turn 90 degrees, the low level of observed separation at inlet should be considered quite good. Similarly, given the high viscous losses experienced in the roughened surface boundary layers, the strength and volume of exit flow is quite surprising. Unfortunately the outer boundary layer still separates and creates a von Karman vortex street.

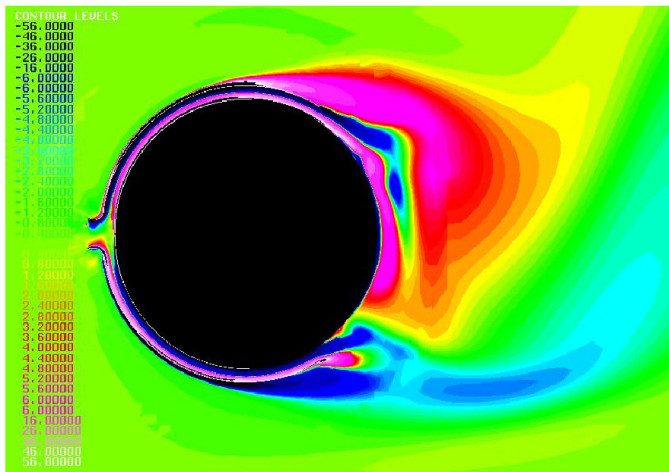


Figure 27: Vorticity Around Sleeve

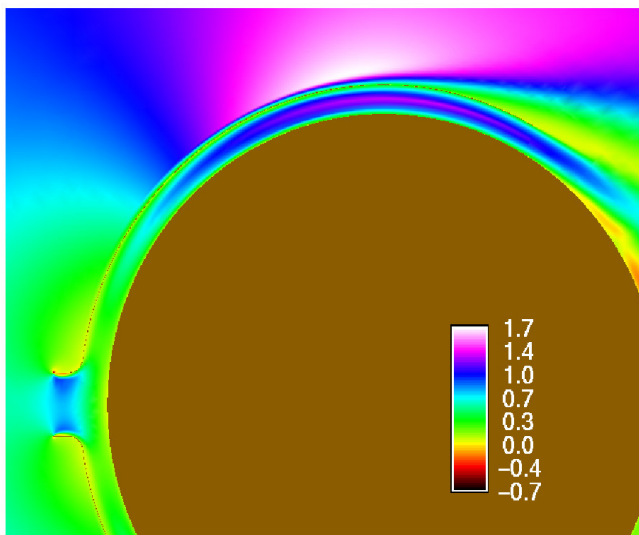


Figure 28: Streamwise Component of Velocity Around Sleeve

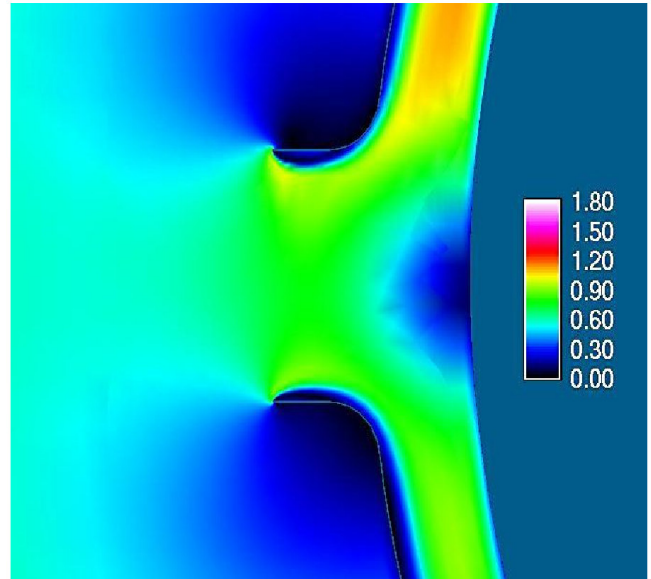


Figure 29: Velocity Magnitude Near Sleeve Inlet

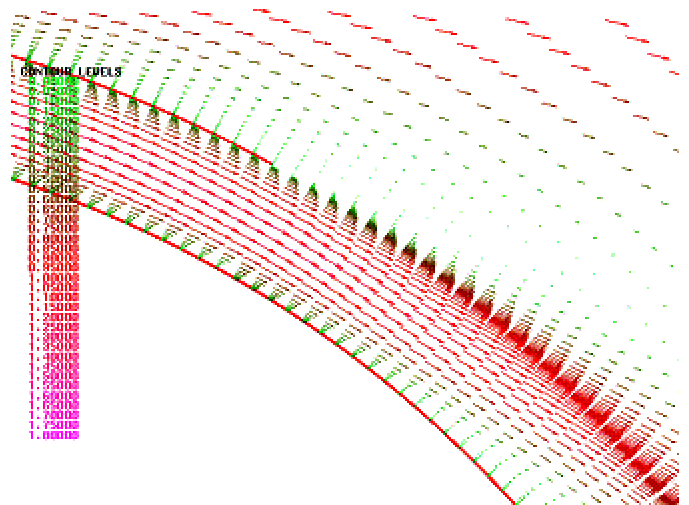


Figure 30: Velocity (Colored by Magnitude) Near Sleeve Outlet

Figures 31 and 32 show the boundary layer thickness and momentum thickness along the spar hull and sleeve. Values plotted for the sleeve inner and outer layers are shown relative to the sleeve location so that boundary layer edges on the hull and sleeve are easily compared (i.e. sleeve inner value is actually $0.05 -$ the boundary layer thickness, and sleeve outer value is $0.05 +$ boundary layer thickness). Note that the sleeve inside and hull boundary layer edges actually touch; indicating that the entire sleeve flow is viscous in nature. Note also that the sleeve outer boundary layer grows rapidly prior to the sleeve end. Indicating separation on the outer surface is imminent. Finally, it should be noted that momentum thickness inside the sleeve is not particularly large, indicating that the channel imposes only modest drag.

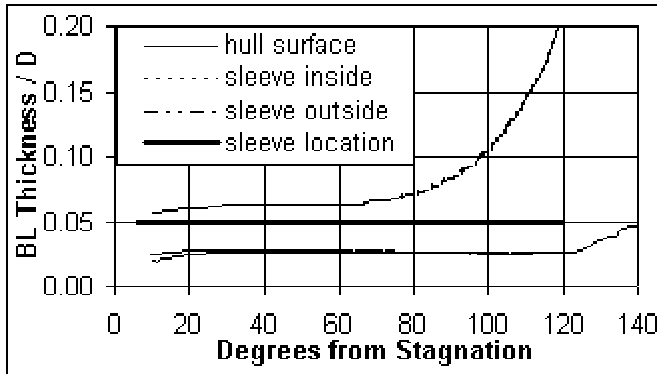


Figure 31: Boundary Layer Thickness on Hull and Sleeve

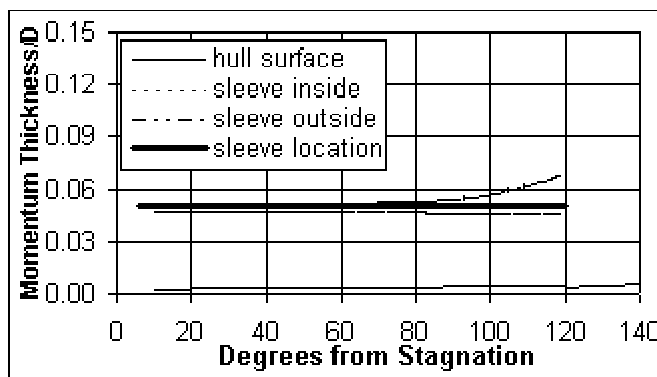


Figure 32: Momentum Thickness on Hull and Sleeve

It is therefore believed that little improvement could be found through detail design shape changes. Some improvement could be possible by increasing the ratio e/t (to inlet more flow), or by reducing t as θ increases (to strengthen the trade from pressure energy to kinetic energy at the channel exit), but neither idea has yet been tested.

RANS predictions of overall VIM performance are given in Figures 33 and 34. The figures show that transverse A/D and mean drag vary with channel exit angle, and that passive injection is not as effective as active injection. Even at the best channel exit angle, transverse A/D is reduced only from about 0.5 (Figure 12) to 0.4. Corresponding mean drag is reduced about 20%, from 1.2 to 1.0. The included off-design simulation points indicate performance is not adversely affected if current and cylinder axis become un-aligned.

Conclusions

RANS was used to study the Vortex-Induced Motions (VIM) of a spar in currents. Roughness models based on first principles physics were introduced, and the code validated using a variety of test cases ranging from flat plates, to flow past fixed cylinders, to spar hulls undergoing VIM. RANS was found to be a viable way to obtain VIM design and analysis data for rough surfaces at super-critical Reynolds numbers.

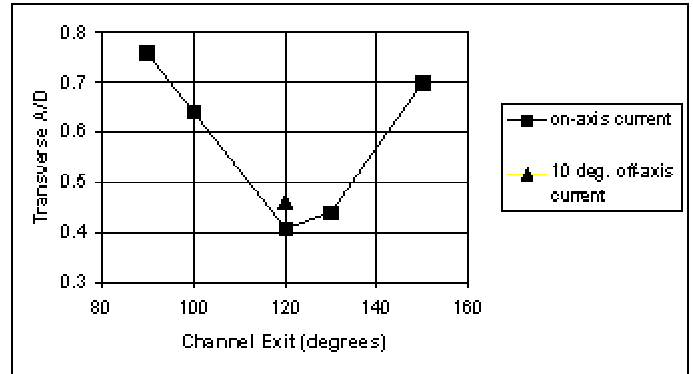


Figure 33: Passive Sleeve Transverse Displacement vs. Exit

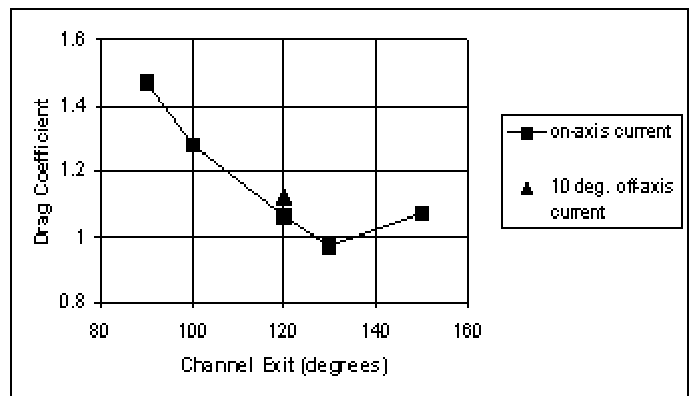


Figure 34: Passive Sleeve Drag versus Exit Angle

The effectiveness of two VIM control strategies was assessed by RANS analyses. Active tangential injection of the boundary layer was found a viable and practical method for alleviating Spar platform VIM. Transverse oscillations can be reduced to almost nothing, and drag was reduced by as much as 4 times. Passive injection can also be used to reduce A/D and drag, but is not nearly as effective as active injection.

References

- [1] Bearman, P., 1984, "Vortex Shedding from Bluff Bodies," *An. Rev. F. Mech.*, **16**, pp. 195-222.
- [2] Blevins, R. D., 1990, *Flow-Induced Vibrations*, Van Nostrand, New York.
- [3] Williamson, C.H.K., 1996, "Vortex Dynamics in the Cylinder Wake," *Am. Rev. of Fluid Mech.*, **28**, pp. 477-539.
- [4] Sarpkaya, T., 1978, "Fluid Forces on Oscillating Cylinders," *J. Waterways, Port, Coastal Eng. Div. ASCE*, **104**, pp 275-290.
- [5] Yeung, R. W., and Vaidhyathan, M., 1993, "Flow Past Oscillating Cylinders," *J. Offshore & Arctic Eng.*, **115**, n. 4.
- [6] Jones, G., Cincotta, J., and Walker, W., 1969, "Aerodynamic Forces on a Stationary and Oscillating Circular Cylinder at High Reynolds Numbers," NASA-TR R-300.

- [7] Lee, C., 2002, "Large Eddy Simulation of Rough-Wall Turbulent Boundary Layers," *AIAA J.*, **40**, n. 10, pp. 2127-2129.
- [8] Kogstad, P., Antonia, R., and Browne, L. 1992, "Comparison of Rough and Smooth-Wall Turbulent Boundary Layers," *J. F. Mech.*, **245**.
- [9] Kogstad, P., and Antonia, R., 1999, "Surface Roughness Effects in Turbulent Boundary Layers," *Exps. in Fluids*, **27**, n. 5, pp. 450-460.
- [10] Grass, A. Stuart, R., and Manisour, M., 1995, "Common Vortical Structure of Turbulent Flows Over Smooth and Rough Boundaries," *AIAA J.*, **31**, n. 5, pp 837-847.
- [11] Perry A., and Joubert, P. 1963, "Rough Wall Boundary Layers in Adverse Pressure Gradients," *J. Fluid Mech.*, **17**, pp. 193-213.
- [12] Perry A., Scifield, W., and Joubert, P. 1969, "Rough Wall Turbulent Boundary Layers," *J. Fluid Mech.*, **37**, pp. 363-413.
- [13] Raspach, M., Antonia, R., and Rajagopalian, S., 1991, "Rough-Wall Turbulent Boundary Layers," *App. Mech. Review*, **44**, n. 1, pp. 1-26.
- [14] Korpus, R., and Falzarano, J.M., 1997, " Prediction of Viscous Ship Roll Damping by Unsteady Navier-Stokes Techniques," *J. of Offshore Mech. and Arctic Eng.*, **119**, no 2., pp. 108-113.
- [15] Korpus, R., Jones, P., Oakley, O., and Imas, L., 2000, "Prediction of Viscous Forces on Oscillating Cylinders by Reynolds-Averaged Navier-Stokes Solver," Transactions of the Int. Soc. of Offshore and Polar Eng., Seattle.
- [16] Korpus, R., Hubbard, B., Jones, P., Stromgren, C., and Bennett, J., 1998, "Hydrodynamic Design of Integrated Propulsor/Stern Concepts by Reynolds-Averaged Navier-Stokes Technique," *Proc. of the 7th Int. Symp. On Practical Design of Ships and Mobile Units*, The Hague.
- [17] Korpus, R., 2004, "Reynolds-Averaged Navier-Stokes in an Integrated Design Environment," Trans. Madrid Deseno de Yates, Madrid.
- [18] Amromin, E., Mizine, I., Crook, L., Day, W., and Korpus, R., 2003, "High Speed Trimaran Drag: Numerical Analysis and Model Tests," *J. of Ship Research*, **47**, n. 2.
- [19] Chen, H.C., and Korpus, R.A., 1993, "A Multi-Block Finite-Analytic Reynolds-Averaged Navier-Stokes method for 3-D Incompressible Flows." *ASME J. of Fluids Eng.*
- [20] Chen, H.C., and Patel, V.C., 1988, "Near-Wall Turbulence Models for Complex Flows Including Separation," *AIAA J.*, **26**, n. 4, pp.641-648.
- [21] Fan, S. Lakshminarayana, B., and Barnett, M., 1993, "Low-Reynolds Number k-e Model for Unsteady Turbulent Boundary Layer Flows," *AIAA J.* **31**, n. 10, pp. 1777-1784.
- [22] Chen, H.C., Patel, V.C., and Ju, S., 1990, "Solutions of Reynolds-Averaged Navier-Stokes Equations for Three-Dimensional Incompressible Flows," *J. of Comp. Physics*, **88**, n.2, pp. 305-336.
- [23] Kumarasamy, S., Korpus, R., and Barlow, J., 1997, "Computation of Noise Due to the Flow Over a Circular Cylinder," *Proceedings of the Second Computational Aeroacoustics (CAA) Workshop on Benchmark Problems*, Tallahassee, Florida, November 4-5, 1996, NASA Conference Publication 3352, pp. 297-303.
- [24] Saki, E., and Biringen, S., 1996, "Numerical Simulation of a Cylinder in Uniform Flow: Application of a Virtual-Boundary Method," *J. Comp. Physics*, **123**, n. 2, pp. 450-465.
- [25] Goldstein, D., Handler, R., and Sinivich, L., 1993, "Modeling a No-Slip Flow Boundary with an External Force Field," *J. Comp. Physics*, **105**, n. 2, pp. 354-366.
- [26] Bandyopadhyay, P, and Watson, R., 1988, "Structure of Rough-Wall Turbulent Boundary Layers," *Phy. Fluids*, **31**, n. 7, pp. 1877-1883.
- [27] Cebeci, T., and Smith, A.M.O., 1974, Analysis of Turbulent Boundary Layers, Academic Press, New York.
- [28] Schlichting, H., 1955, Boundary Layer Theory, 7th edition, McGraw-Hill, New York.
- [29] Ding., Z., Batasubramanian, S., Lokkan, R., and Yung, T.-W., 2004, "Lift and Damping Characteristics of Bare and Straked Cylinders at Riser Scale Reynolds Numbers," Offshore Tech. Conf., Houston.
- [30] Hover, F., Techet, A., and Triantafyllou, M, 1998 "Forces on Oscillating Uniform and Tapered Cylinders in Cross Flow," *J. F. Mech.*, **000**, pp 1-18.
- [31] Liu, G., Devlin, P., and Kwan, C., 2004, "Mooring Design for Spar VIM in West Africa," *Proc. Offshore Tech. Conf.*
- [32] Shu, H., and Allen, D., 2000, "Active Apparatus and Method for Reducing Fluid Induced Stresses by Introduction of Energetic Flow into Boundary Layer around an Element", U.S. Patent 6551029.
- [33] Schultz, K., Kallinderis Y. and Liapis, S. (2000) Active control of Spar Vortex-Induced Motions, unpublished report.
- [34] Brown, N, Grinius, V., and Shaar, K., 2000, "Water Jet VIV Reduction", OMAE Conf., New Orleans, Oral Presentation.
- [35] Shu, H., and Allen, D., 2001, "Passive Apparatus and Method for Reducing Fluid Induced Stresses by Introduction of Energetic Flow into Boundary Layer around Structures", U.S. Patent 20020066570.